Geometric frustration in polygons of polariton condensates creating vortices of varying topological charge

Tamsin Cookson[1,2], Kirill Kalinin[1,3], Helgi Sigurdsson[1,2],
Julian D. Töpfer[1,2], Sergey Alyatkin[1], Matteo Silva[2], Wolfgang
Langbein[4], Natalia G. Berloff[1,3], and Pavlos G. Lagoudakis[1,2*]

[1]*Skolkovo Institute of Science and Technology,*
Skolkovo 143025, Russian Federation

[2]*Department of Physics and Astronomy, University of Southampton,*
Southampton, SO17 1BJ, United Kingdom

[3]*Department of Applied Mathematics and Theoretical Physics,*
University of Cambridge, Cambridge CB3 0WA, United Kingdom and

[4]*School of Physics and Astronomy, Cardiff University,*
The Parade, Cardiff CF24 3AA, United Kingdom

(Dated: January 18, 2021)

Abstract

Vorticity is a key ingredient to a broad variety of fluid phenomena, and its quantised version is considered to be the hallmark of superfluidity. Circulating flows that correspond to vortices of a large topological charge, termed *giant vortices*, are notoriously difficult to realise and even when externally imprinted, they are unstable, breaking into many vortices of a single charge. In spite of many theoretical proposals on the formation and stabilisation of giant vortices in ultra-cold atomic Bose-Einstein condensates and other superfluid systems, their experimental realisation remains elusive. Polariton condensates stand out from other superfluid systems due to their particularly strong interparticle interactions combined with their non-equilibrium nature, and as such provide an alternative testbed for the study of vortices. By non-resonantly exciting an odd number of polariton condensates at the vertices of a regular polygon, we observe the formation of a stable discrete vortex state with a large topological charge as a consequence of antibonding frustration between nearest neighbouring condensates.

---

* P.Lagoudakis@skoltech.ru; N.G.Berloff@damtp.cam.ac.uk

Quantised vortices are fundamental topological objects playing an important role in branches of physics ranging from superfluids and superconductors to high energy physics and optics. They exist in classical matter fields, described by a complex-valued function $\Psi(\mathbf{r}, \mathbf{t}) = \sqrt{\rho(\mathbf{r}, \mathbf{t})} \exp[iS(\mathbf{r}, \mathbf{t})]$, as singular points in two-dimensions, or lines in three-dimensions, where $\rho = 0$ and the phase S winds around in multiples of 2π. The winding of a quantised vortex, also called topological charge, is the integer defined as $m = (1/2\pi) \oint_C \nabla S \cdot d\mathbf{l}$, where C is the closed contour around the vortex singularity. Although the formation, structure, dynamics, and turbulence of quantised vortices has been subject of intense research [1] many fundamental aspects of vortex dynamics such as its effective mass [2] and applicable forces [3] are still not fully understood. Vortex motions, even in the simplest configurations, such as the advection of a single vortex of unit charge by a constant superflow have intrigued the scientific community [4].

The creation of multiply quantised vortices, or giant vortices, in ultra-cold atomic Bose-Einstein condensates (BECs) has challenged researchers [5–8] since a multiply-charged vortex, both in a uniform and sufficiently large condensate [9], as well as in a trapped condensate [10], is dynamically and thermodynamically unstable and tends to break into an array of singly-charged vortices [11]. Numerous theoretical proposals address how to stabilise multiply charged vortices such as, exploiting stronger than harmonic confinement and fast rotation [6, 7], using a near-resonant laser beam [8], introducing a second species of BEC [12], organising spatiotemporally modulated interactions [13], or with spin-orbit coupling [14]. However, evidence that many vortices can merge and stay stable as a single giant vortex remains elusive, as is the case in other quantum fluid systems such as superfluid helium-3 and 4 [16, 17].

In mesoscopic superconducting materials vortices of large topological charge have already been reported [18–20] with numerical simulations corroborating the evidence, since the available experimental techniques provided limited probing of the vortex core [20–22]. In many respects, these vortices have similar physics to giant vortices in atomic BECs but with external rotation controlled through an applied magnetic field. By increasing the amplitude of the magnetic field, a vortex of multiplicity three was experimentally observed in a strongly confined type-II superconductor [23]. Apart from quantised vortices that exist on a non-zero, and usually uniform background, a new class of vortices was introduced theoretically and achieved experimentally in optics and atomic physics: those found in optical

lattices of ultra cold BECs or periodic photonic structures of light called discrete vortex solitons (DVSs) [24–26]. The core of such vortices lies on a negligible density background and their phase winds to provide spatially localised circular energy flows between lattice sites. In previous experimental realisations, the phase corresponding to multiple singly-charged vortices was directly imprinted by laser beams that resulted in stationary DVSs [27], and a double-charged vortex was shown in a hexagonal photonic lattice [28]. Similarly, a ring network of dissipatively coupled lasers [29, 30] or optical parametric oscillators [31] may establish a phase winding as an excited state. Non-equilibrium condensates, on the other hand, offer alternative mechanisms for stabilisation of giant vortices such as inward particle fluxes toward the trapped condensate's centre [32].

Geometric frustration (henceforth *frustration*) occurs in magnetic systems when the relative arrangement of spins posses multiple degenerate ground state configurations [33]. It has been intensely studied since 1950, when its formation was presented in a two dimensional Ising net in a triangular lattice [34], and later in the three dimensional pychlore lattice [35]. Frustration can be engineered into systems by controlling the geometry and coupling strength between spins. Atoms trapped in a two dimensional optical lattice were able to simulate different regimes of the XY Hamiltonian [36]. Similarly, frustration has also been seen in lattices of coupled laser systems, a negatively coupled triangular lattices with $\pm 2\pi/3$ phase locking has been observed, leading to singly-quantised vortices and alternate chirality in the lattice [37]. In strongly-coupled microcavity polariton lattices, frustration caused the observation of a flat band in the dispersion of a Lieb lattice [38].

In this article, we realise frustrated polygons of polariton condensates as a platform to create and study circulating currents leading to vortices of varying topological charge. Polaritons are solid-state quasiparticles that result from the hybridisation of strongly coupled excitons and photons in semiconductor microcavities. At low densities, they behave as short-lived bosons (several picoseconds lifetime) that can undergo a power-driven phase transition into a non-equilibrium condensate [39] remaining indefinitely stable under continuous non-resonant excitation. Polariton condensates and related phenomena have been the subject of intense investigation for some time [40, 41], including quantised vortices and their dynamics [42–51]. Unlike DVSs in purely optical systems or photonic crystals, where the phase winding comes from the laser, in polariton graphs, vortices form spontaneously during condensation. In this respect, they are closer to vortices in atomic condensates, but
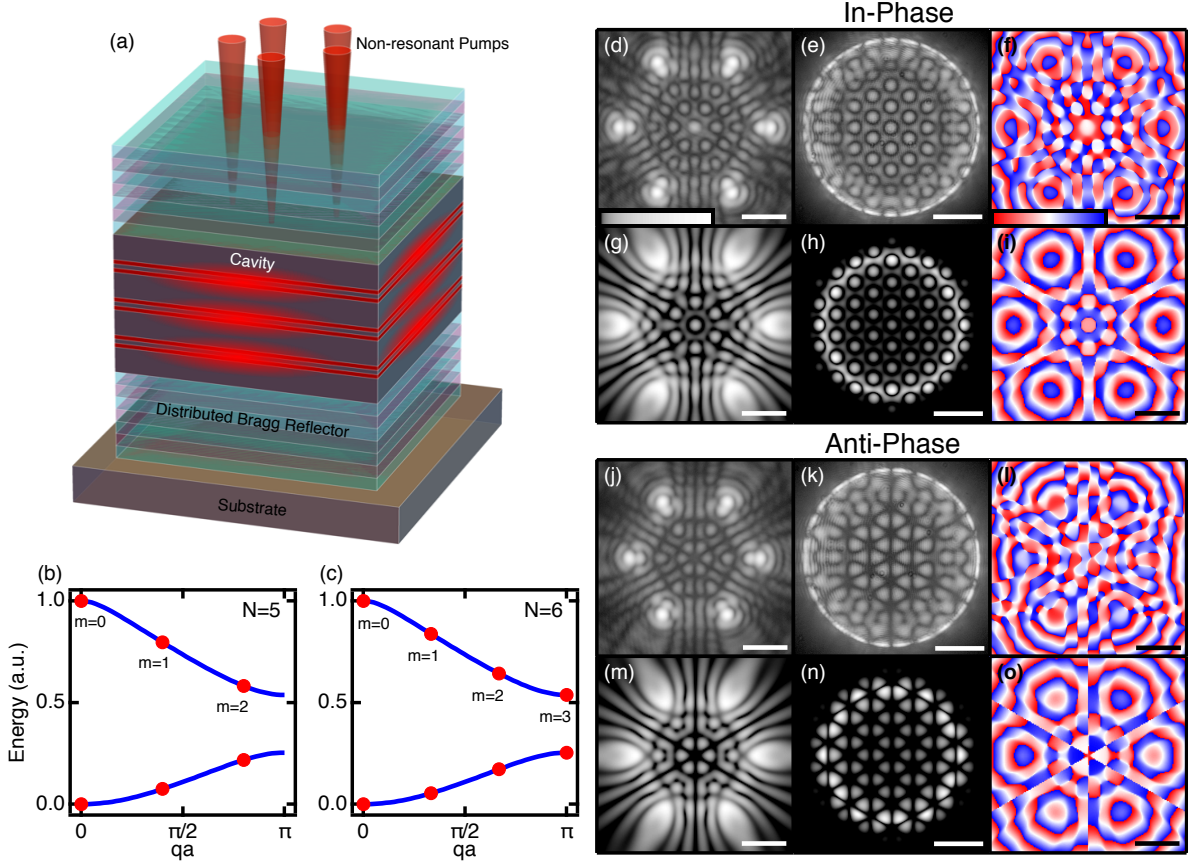
FIG. 1. (a) Schematic showing a quantum well microcavity. Non-resonant lasers (red cones) at normal incidence create polariton condensates at their respective locations. (b,c) Example reduced Brillouin zone energies of angular Bloch modes (red dots) in an $N = 5$ and $N = 6$ polygon respectively. Blue curves show band structure in the thermodynamic limit. (d,j) Experimental condensate photoluminescence in real-space and (e,k) Fourier-space in a hexagon geometry, with radii $R = 16.9$ μm and $R = 14.7$ μm, showing in-phase and anti-phase locked condensates respectively. (f,l) Corresponding experimentally extracted real-space polariton phase maps. (g-i) and (m-o) show simulations of the steady state polariton condensate wavefunction $\Psi(\mathbf{r}, t)$ using the driven-dissipative Gross-Pitaevskii equation in the in-phase and anti-phase locked configuration respectively. (g,m) Real-space density $|\Psi(\mathbf{r})|^2$, (h,n) Fourier-space density $|\hat{\Psi}(\mathbf{k})|^2$, (i,o) and phase $\arg(\Psi(\mathbf{r}))$. Image parameters for all panels are noted in SI, Section VI.

as we demonstrate, they do not require any external stirring, and even multiply charged vortices are fully stabilised in the non-equilibrium polariton system. Also, unlike vortices in ultra-cold atomic BECs, polariton giant vortices generate spiral velocity profiles towards the

vortex centre [52]. Here, we consider ballistically expanding condensates at the vertices of a regular polygon. Figure 1(a) shows a schematic of the microcavity system with a pentagon non-resonant pumping geometry (red cones). The term "ballistically expanding" means that the condensates are not confined in a potential minimum but are instead gain-localised due to the tightly focused ($\sim$2 μm full-width-half-maximum) optical excitation beams feeding particles into the condensates. The advantage of such non-Hermitian localisation is the coherent polariton outflow from each pump spot, causing strong interference with neighbouring condensates [53].

By incrementally raising the polygon's pump power, polaritons eventually undergo condensation and the system is described by an order parameter $\Psi(\mathbf{r}, t)$ belonging to a polariton mode with the highest optical gain. By tuning the separation distance between pump spots, one can control the coupling between nearest neighbours [54], and therefore, the phase configuration across the polygon. Although we present results on a single macroscopic coherent polariton condensate across the entire polygon, we will refer also to the vertices of the polygon as "individual" condensates, which can interfere and synchronise. The modes of the entire system belong to a point symmetry operator $\mathcal{C}_N$ of cyclic N-fold rotations, where N is the number of condensates (vertices in the polygon). Being rotationally periodic, one can apply Bloch's theorem along the planar azimuthal angle φ such that $\Psi_{q,n}(\mathbf{r}) = e^{iq\varphi} u_{q,n}(\mathbf{r})$ where $u_{q,n}(r, \varphi) = u_{q,n}(r, \varphi + 2\pi/N)$ is the Bloch mode of the system and $q = 2\pi m/L$ is the quasimomentum along the polygon's circumcircle for $m \in \mathbb{Z}$ satisfying $|m| \leq N/2$, and $L = Na$ being the length of the polygon's circumcircle. In Fig. 1(b,c) we show example two energy branches of the discrete Bloch modes (red dots) for $N = 5$ and $N = 6$ polygon respectively in the reduced Brillouin zone. The blue curves denote the bands in the thermodynamic limit $N \to \infty$.

Previously, it was shown that condensation of ballistically expanding condensates can be correlated with the ground state configuration of the XY Hamiltonian, $\mathcal{H}_{XY} = -\sum_{ij} J_{ij} \cos(\theta_i - \theta_j)$, where J_{ij} and $\theta_{ij} = \theta_i - \theta_j$ are the coupling strength and the relative phase between condensates i and j respectively [54, 55]. The coupling strength J_{ij} depends on the pump power, the distance between condensates, $d_{ij} = |\mathbf{r}_i - \mathbf{r}_j|$, and the in-plane wavenumber k_c of the condensate polaritons expanding from their respective pump spots [53], all of which can be controlled by tuning the pumping power and geometry using spatial light modulators. If one tunes the system to have $J_{ij} > 0$, then the coupling is said to be ferromagnetic

and a solution with maximum polariton gain has all condensates locked in-phase; whereas if $J_{ij} < 0$ the coupling is said to be antiferromagnetic and the condensates try to be in anti-phase (π phase). In a regular polygon with uniform nearest neighbour interactions, the XY Hamiltonian becomes cyclic $\mathcal{H}_{XY} = -J\sum_{i=1}^{N} \cos\theta_{i,i+1}$, with the boundary condition $\theta_1 = \theta_{N+1}$. It is then understood that in-phase and anti-phase configurations are simply modes with quasimomentum $q = 0$ and $q = N\pi/L$, at the centre and edges of the crystal Brillouin zone respectively where polaritons have been observed to preferentially condense into [56]. Correspondingly, Bloch modes between the centre and the edges of the Brillouin zone, i.e. $0 < |m| < N/2$, are simply vortices of winding number m.

When $J < 0$, and N is odd, the edges of the Brillouin zone become forbidden and polaritons condense instead into the state closest to the edge which maximises the gain. For odd numbered N this state is $\theta_{i,i+1} = \pm(N-1)\pi/N$. Interestingly, a superposition of the two counter-propagating modes is not observed as stable solution of the frustrated polygon system, but instead, a breaking of the parity symmetry occurs with the formation of a net polariton current along the polygon circumcircle. Such symmetry breaking can only be attributed to nonlinear effects in the condensate and has previously been reported in both experiment [57, 58] and theory [59–61]. Solutions of lower vorticity (further away from the Brillouin zone edge) are also stable and observable in measurements even though they do not correspond to the highest gain of the XY model. Here, we report on the observation of these parity-breaking solutions forming discrete vortex (or simply *vortex*) states in polygon configurations of polariton condensates with winding number m. In the simplest case of $N = 3$, the formation of a $|m| = 1$ vortex ($\theta_{i,i+1} = \pm 2\pi/3$) was observed in 2016 [54].

To experimentally control the condensate phase configurations we inject equidistant polariton condensates at the vertices of a regular polygon. We preclude any correlation between the phase of the pumping source and the realised phase configurations, by pumping polariton condensates using non-resonant continuous wave optical excitation on a multiple InGaAs quantum well semiconductor microcavity [62] (see Fig. 1(a)). For a description of the sample, and excitation and detection scheme, see Section I of the Supplementary Information (SI). In addition, we simulate the dynamics of the polariton condensates using the two-dimensional driven-dissipative Gross-Pitaevskii equation [63, 64] written for the condensate
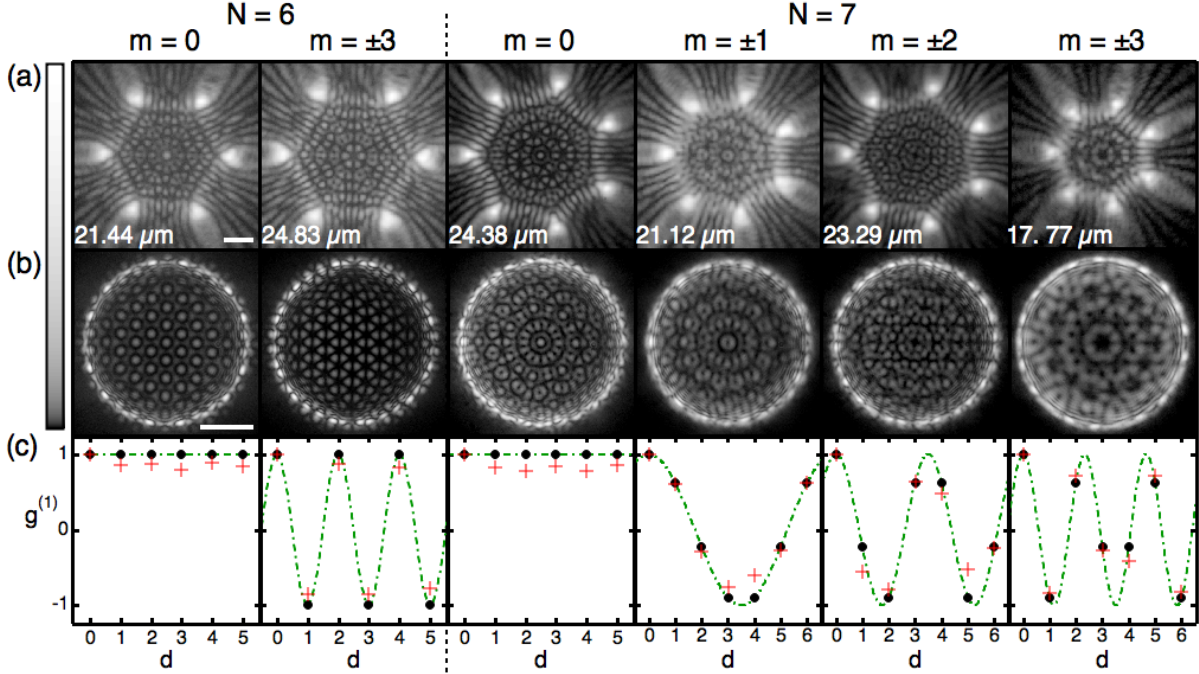
6

FIG. 2. (a,b) Real- and Fourier-space imaging of a hexagon and heptagon in different coupling configurations achieved by tuning the radius. Two leftmost columns show condensation of a hexagon into in-phase ($m = 0$) and anti-phase ($m = 3$) configurations whereas four rightmost columns show in-phase ($m = 0$) and vortex-formation ($m = \pm1, \pm2, \pm3$) of a heptagon. (c) Extracted (red crosses) and calculated (black dots) mutual first-order coherence $g^{(1)}$ versus parameter d extracted from the interferogram between condensates for different polygon configurations. The values of $g^{(1)}$ lie upon the continuous function (green dot-dashed line) given by $g^{(1)}(x) = \cos(2\pi m x/N)$, where x has replaced the discrete parameter d. The point at $d = 0$ corresponds to the autocorrelation of the condensate wavefunction at zero time-delay and is set as $g^{(1)}(0) = 1$. The radii of the polygon are written in the bottom left hand corner of the real-space images in (a).

wavefunction, $\Psi(\mathbf{r}, t)$, and the rate equation of the hot exciton reservoir, $X(\mathbf{r}, t)$:

$$i\hbar\frac{\partial\Psi}{\partial t} = \left[(i\Lambda - 1)\frac{\hbar^2}{2m^*}\nabla^2 + \alpha|\Psi|^2 + gX + GP(\mathbf{r}) + \frac{i\hbar}{2}(RX - \gamma)\right], \qquad (1)$$

$$\frac{\partial X}{\partial t} = -\left(\Gamma + R|\Psi|^2\right)X + P(\mathbf{r}), \qquad (2)$$

where m^* is the polariton effective mass, α is the polariton-polariton interaction strength, g is the interaction strength of polaritons with the exciton reservoir feeding the condensate, G is the interaction strength of polaritons with the dark background of inactive excitons which

do not scatter into the condensate, R is the scattering rate of reservoir excitons into the condensate, $P(\mathbf{r})$ is the non-resonant pump(s), γ is the rate of losses of condensed polaritons through the cavity mirrors, Γ is the rate of redistribution of reservoir excitons between the different energy levels, and Λ is a phenomenological energy relaxation parameter [65], (simulation parameters can be found in SI, Section II).

We start by investigating stationary states characterised by in-phase and anti-phase bonding between condensates in the absence of frustration. Figures 1(d-f) show experimental results for real-space, Fourier-space (k_x-k_y momentum plane), and phase of the polariton photoluminescence (PL) in a hexagon of radius $R = 16.9$ µm. The coupling is clearly distinguishable as $J > 0$ from the odd number of bright fringes between the vertices, evidencing in-phase locking. Figures 1(j-l) show same measurements for a hexagon of radius $R = 14.7$ µm, where we now observe an even number of fringes between the vertices ($J < 0$), evidencing anti-phase locking. Figures 1(g-i) and (m-o) show corresponding simulations of the steady state, in-phase and anti-phase locked, polariton condensate wavefunction using the driven-dissipative Gross-Pitaevskii equation in agreement with experimental observations. Other polygon geometries for both in-phase and anti-phase configurations of the condensates are given in the SI, Section III. We note that all image parameters (scales) are given in SI, Section VI.

We investigate the system where we time-integrate over multiple instances of the condensate. Here, we are unable to directly observe the frustrated current in one direction, or the other, due to the stochastic choice of chirality during condensation and so, relative condensate phase readout through interferometric techniques averages out. In-phase and anti-phase states with $\theta_{i,i+1} = 0$ or π are the notable exception which are observable in averaged measurements because they are non-degenerate. Nevertheless, as we describe in the following, two stochastically appearing counter-circulating currents ($\pm m$) give rise to a spatially oscillating coherence pattern that allows us to uniquely determine the vortex state $|m|$ in averaged measurements. The first-order mutual coherence function,

$$g_{ij}^{(1)} = \frac{\langle \Psi_i^* \Psi_j \rangle}{\sqrt{\langle |\Psi_i|^2 \rangle \langle |\Psi_j|^2 \rangle}} \qquad i,j \in \{1,\ldots,N\}, \tag{3}$$

describes the coherence properties between two condensates i and j with wavefunctions $\Psi_{i,j}$ in a polygon of N coupled condensates. In the following, we assume that nodes are labelled sequentially $1, 2, ..., N$ along the polygon. For a circulating current of charge m along the

polygon satisfying $\langle|\Psi_i|^2\rangle = \langle|\Psi_j|^2\rangle$ the complex coherence function is given by $g^{(1)}(d) = \exp{(i2\pi md/N)}$ where $d = |i - j|$. In the case of equal probabilities of the two stochastically appearing degenerate counter-propagating currents with charge $\pm m$ the mutual coherence function becomes a standing wave,

$$g^{(1)}(d) = \cos{(2\pi md/N)}. \tag{4}$$

By extracting the mutual coherence function $g^{(1)}(d)$ along the polygon nodes we are able to determine the charge $|m|$ (or alternatively Bloch mode) of the stochastically appearing degenerate currents. In Fig. 2(c) we show the measured (red crosses) values of the mutual coherence function for the systems shown in Figs. 2(a,b). The first column displays the in-phase hexagon with all relative phases at zero and a high coherence. The second column shows an anti-phase hexagon again with a high coherence but now interchanging between $+1$ and -1, reflecting the phase jumps along the polygon in the anti-phase configuration. The black dots in the coherence graphs indicate the value calculated by Eq. (4) and the green dashed line represents the $g^{(1)}$ function replacing d for a continuous variable.

The most interesting phase configuration is predicted for an odd number of condensates in the frustrated regime $(J < 0)$, shown for a heptagon in the final three columns with the fourth column depicting a phase difference of $\theta_{i,i+1} = \pm 2\pi/7$ indicating a vortex of $|m| = 1$, the fifth column has $\theta_{i,i+1} = \pm 4\pi/7$ for a vortex of $|m| = 2$, and the final column has $\theta_{i,i+1} = \pm 6\pi/7$ for a vortex of $|m| = 3$. The real values of the $g^{(1)}$ are extracted from interferograms between the selected condensates with $d = 0$ representing the interference of a condensate with itself. We note that the in-phase heptagon $(m = 0)$ is displayed in the third column and has a high coherence between all condensates. The coupling J in the polygon is controlled by altering the radius of the polygon, which we detail in the SI, Section V. The extracted data (red crosses) is in good agreement with the predicted values. It is instructive to compare the extracted coherence properties of the anti-phase state of the hexagon with the frustrated states of the heptagon. In the former, clear switching of $g^{(1)}$ between -1 and 1 can be seen which gives a total of three full periods around the hexagon, whilst for the circulating states with $\theta_{i,i+1} = \pm 2\pi/7, \pm 4\pi/7, \pm 6\pi/7$ we observe one, two and three total periods around the heptagon respectively. We also note that for the circulating states in the heptagon the discrete values do not occur at the peak or trough of the wave, except for the case of $d = 0$ but at intermediary values due to the averaged phase

9

of the circulating state. These results evidence nontrivial phase configuration appearing in the polygon polariton condensates which can be attributed to frustration and spontaneous onset of a circulating polariton current. We point out that our results are in agreement with the ensemble averaged measurements performed on lattices of coupled laser systems [66].

We provide further evidence on the formation of a circulating polariton current by investigating condensation in the single shot regime where a single instance of the condensate polygon is excited and measured. Figure 3(a) shows the experimental real-space PL of a frustrated pentagon ($N = 5$), wherein we observe an even number of interference fringes between neighbouring condensates. Figure 3(b) shows the Fourier-space PL where we observe an absence of radial nodal lines in contrast to Fig. 1(k). We point out that the presence of radial nodal lines in the Fourier space PL would evidence anti-phase locked condensates, corresponding to standing wave formation along the polygon and a zero-net current. Here, however, the lack of nodal lines suggests the presence of a net particle current along the polygons edge. For comparison, we show numerical simulations in Figs. 3(e,f) of the real- and Fourier-space density of the condensate wavefunction resulting in a stable discrete vortex solution with a winding $m = -1$. We note that the winding number sign in simulation is stochastically determined from random initial conditions.

Although the frustrated vortex regime can be classified from the nontrivial interference patterns appearing in the real- and Fourier-space PL, it does not concretely verify the presence of a vortex state. We therefore resolve the spatial phase distribution of the vortex using off-axis digital holography [42] (see SI, Section I). During condensation, the vortex formation stochastically results in either clock- or anticlock-wise winding of the phase along the polygon edge. Averaging over several condensate instances would therefore skew direct measurement of the phase. Instead, in order to view the vortex state, we utilise a single condensate realisation detection scheme, whereby each image of the polygon is the result of a single instance of the condensate formation. Figure 3(c) shows the experimental phase of the condensates with a $m = -1$ vortex, extracted from its interferogram, where it can be seen to spiral about the polygon's centre. Figure 3(d) shows a zoomed in the region corresponding to the black dashed square in Fig. 3(c). Figures 3(g,h) show a corresponding real-space phase map from the simulation in Fig. 3(e,f). To further verify that the entire condensate possesses a circulating current we directly measure the phase coming from the bright emission spots at the polygon vertices where most of the condensate resides. The
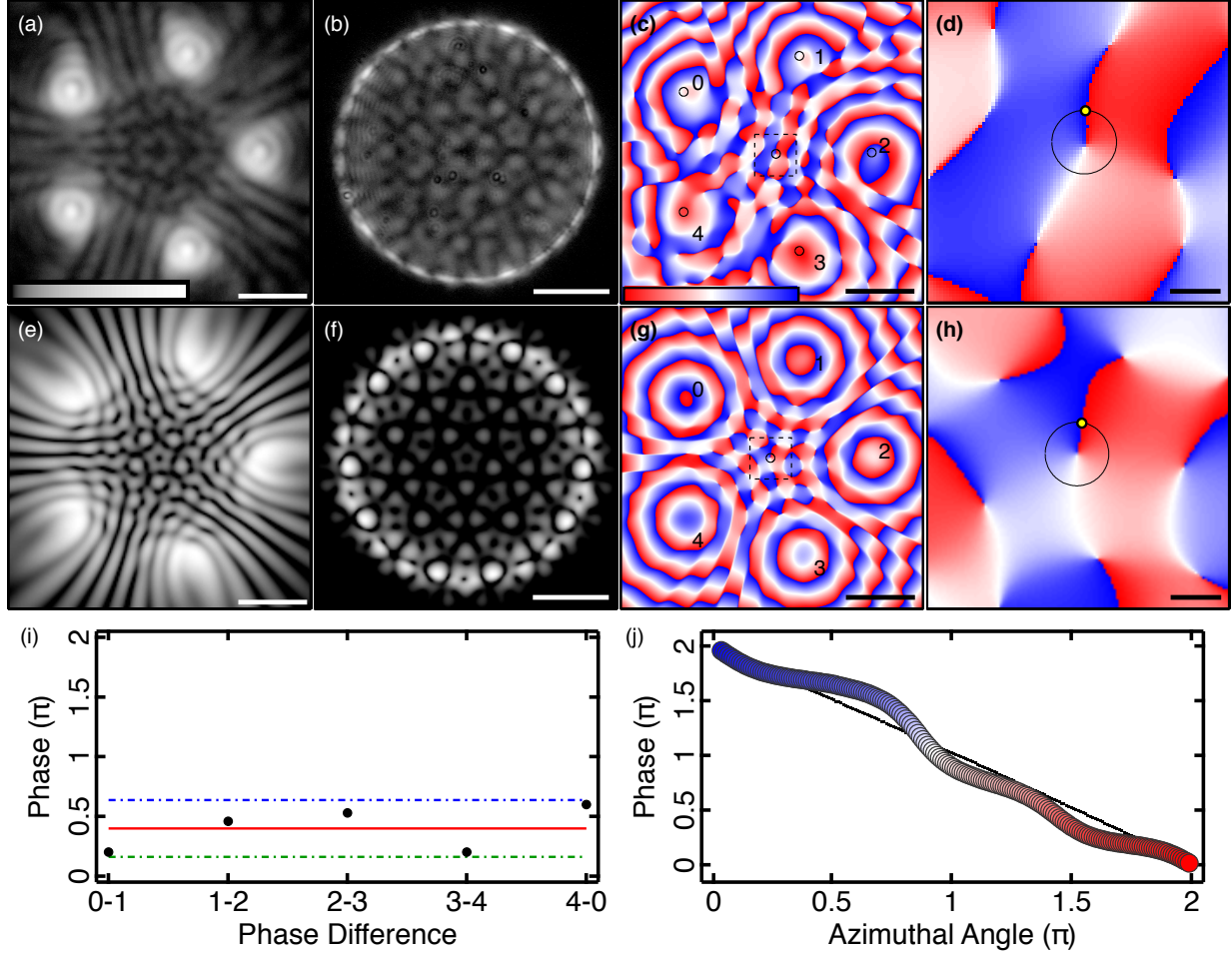
FIG. 3. Pentagon condensate with a charge $m = -1$ vortex. (a) Experimental real-space PL, (b) Fourier-space PL, and (c,d) phase extracted from interferometry from a single instance of the condensate. Simulated steady state $m = -1$ vortex wavefunction (e) real-space density, (f) Fourier-space density, (g,h) and phase. (d,h) Zoomed in regions of the dashed squares in (c,g) respectively. (i) Phase difference between adjacent condensates (black dots) around the polygon extracted from the black circles in (c). The red line is the expected phase difference of $\theta_{i,i+1} = 2\pi/5$. Green and blue dash-dotted lines mark the maximum deviation. (j) Line profile extracted along the black circle in (d,h) demonstrating a full 2π phase winding. Yellow dots correspond to azimuthal angle equal to zero. Experimental data is represented by the coloured disks and numerical simulation by the black curve.

experimentally measured relative phase between neighbouring condensates is demonstrated with black dots in Fig. 3(i), which are extracted from the regions denoted by black circles
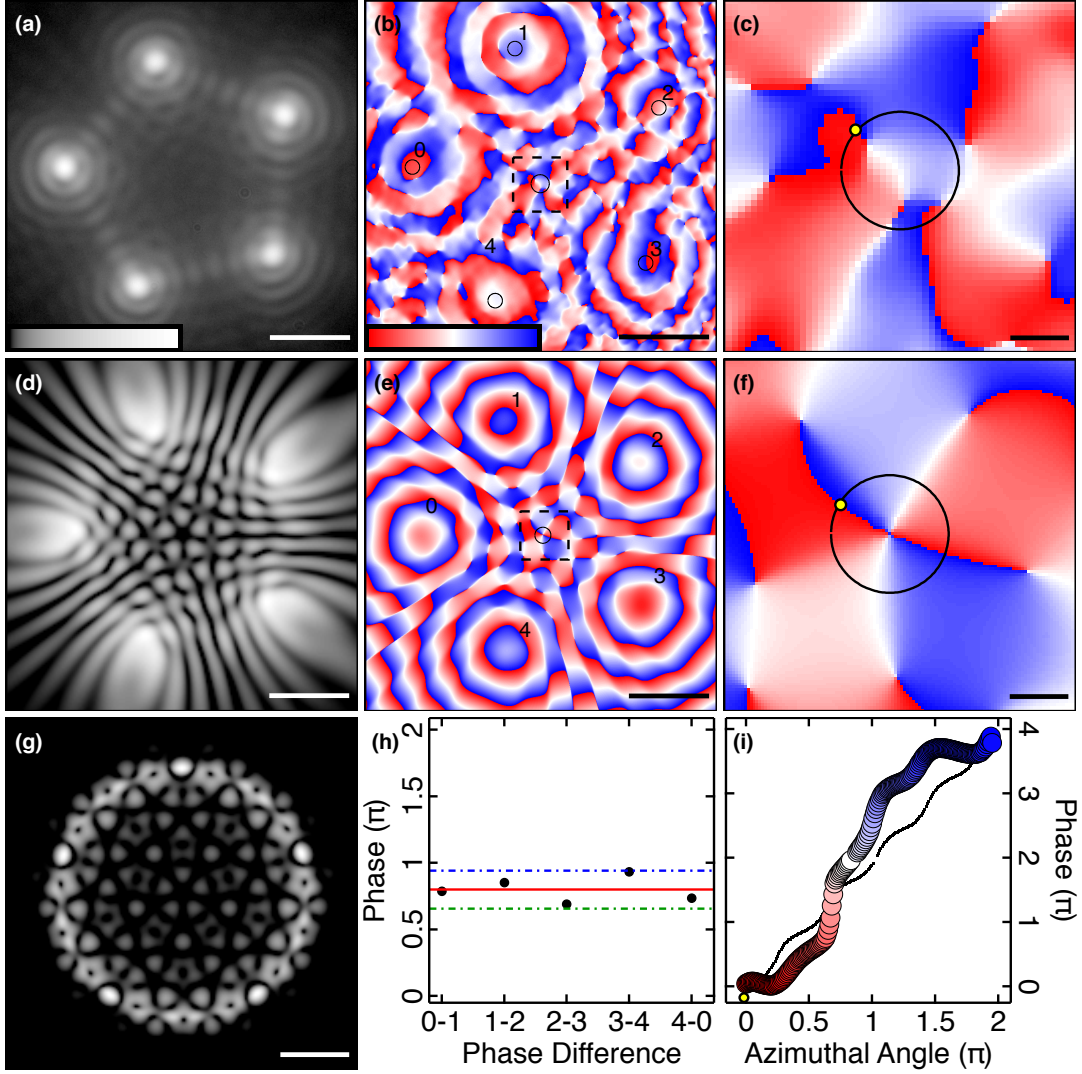
11

FIG. 4. Pentagon condensate with a charge $m = 2$ vortex. (a) Experimental real-space PL and (b,c) phase extracted from interferometry from a single instance of the condensate. Simulated steady state $m = 2$ vortex wavefunction (d) real-space density, (g) Fourier-space density, (e,f) and real space phase. (c,f) Zoomed in regions of the dashed squares in (b,e) respectively. (h) Phase difference between adjacent condensates (black dots) around the polygon extracted from the black circles in (b). The red line is the expected phase difference of $\theta_{i,i+1} = 4\pi/5$. Green and blue dash-dotted lines mark the maximum deviation. (i) Line profile extracted along the black circle in (c,f) demonstrating a full 4π phase winding. Yellow dots correspond to azimuthal angle equal to zero. Experimental data is represented by the coloured disks and numerical simulation by the black curve.

in Fig. 3(c). The relative phases are close to the expected vortex value of $\theta_{i,i+1} = 2\pi/5$ (red line) with a maximal deviation of 0.6 radians (blue and green dash-dotted lines). Line profiles taken along the black circles in Figs. 3(d,h) are shown in Fig. 3(j) and unveil a full 2π phase winding about the vortex core, where the experimental data is represented by the coloured disks and the numerical simulation by the black curve.

In Fig. 4 we show an experimental realisation of a frustrated pentagon condensate containing a vortex of charge $m = 2$. Figure 4(a) shows the experimental real-space PL wherein we again observe an even number of interference fringes between neighbouring condensates in real-space. Figures 4(b,c) show the phase of the polygon condensate which can be seen to wind about its centre characterised by two phase singularities at the core. Figures 4(d-g) show a corresponding numerical simulation of a steady state $m = 2$ vortex. In Fig. 4(h) we show the experimentally measured relative phase between neighbouring condensates, extracted from the regions denoted by black circles in Fig. 4(b), revealing the expected double vortex phase difference of $\theta_{i,i+1} = 4\pi/5$ (red line) with a maximal deviation of 0.45 radians (blue and green dash-dotted lines). Line profiles taken along the black circles in Figs. 4(c,f) now unveil a full 4π phase winding about the vortex core (see Fig. 4(i)). We observe that the line profile of the simulation (black dots, Fig. 4(i)) is not straight but has small oscillations along the azimuthal angle. We attribute this to the system not being cylindrically symmetric, and so, angular momentum is no longer a good quantum number and the 2D angular harmonics $e^{iw\varphi}$ should be replaced by angular Bloch solutions $u_{q,n}(r, \varphi)e^{iq\varphi}$ which in general possess more complex phase structure leading to the extra modulation of the phase seen in simulations, similar to what has been seen for vortices in optical lattices like in Ref. [26]. We note that we do not externally imprint the vortex phase [67, 68], but we rather control the dynamics of the coupling between condensates, which leads to the spontaneous formation of these vortices. In Section IV in the SI we estimate the probability of vortex formation through simulations of varying polygon radii, and irregularities.

We observe that in some instances for frustrated odd-numbered polygons the condensates do not successfully "agree" with each other on which direction to form a current. This leads to a state which does not have a single central vortex but rather forms a vortex-antivortex pair as shown in Fig. 5. Figure 5(a,b) shows the experimental real-space magnitude of the PL and phase respectively. The diagonal dashed lines are guide to the eye marking a split in density across the condensate polygon. Figure 5(c) shows a zoomed in region corresponding
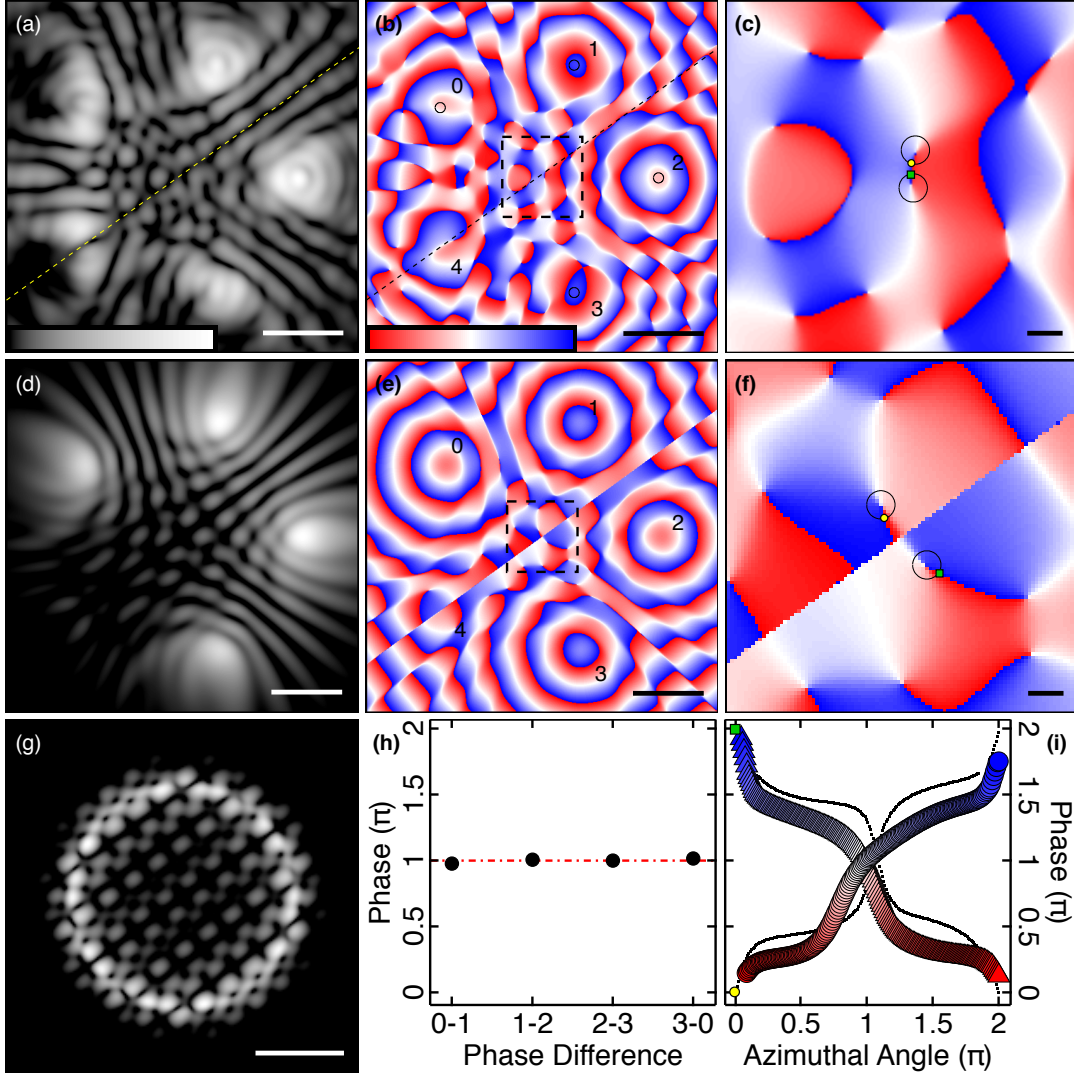
FIG. 5. Pentagon condensate with a $|m| = 1$ vortex-antivortex pair. (a) Experimental real-space PL and (b,c) phase extracted from interferometry from a single instance of the condensate. Simulated steady state vortex-antivortex wavefunction (d) real-space density, (e,f) phase, and (g) Fourier-space density. (c,f) Zoomed in regions of the dashed squares in (b,e) respectively. (h) Phase difference between different condensates (black dots) in the polygon extracted from the black circles in (b). (i) Line profiles extracted along the two dashed circles in (d,h). Yellow and green markers correspond to azimuthal angle equal to zero. Experimental data is represented by the coloured disks and numerical simulation by the black-dotted lines.

to the black dashed square. A vortex-antivortex pair can be observed with cores separated by ~ 1 μm. Figures 5(d-g) show a corresponding numerical simulation of a condensate

14

steady state with a vortex-antivortex pair, obtained by displacing pump spot number 4 in the pentagon by 2.8 μm radially outwards. Figure 5(h) shows that the measured phase difference between the vertices 0-1, 1-2, 2-3, and 0-3 is equal to π whereas the phase of condensate 4 is not well defined due to destructive interference, fracturing it into two parts. Line profiles taken along the black circles in Figs. 5(c,f) unveil an opposite 2π phase winding about each of the vortex cores (see Fig. 5(i)).

We lastly discuss some sources of discrepancies appearing between theory and observations. We firstly underline that the mean-field model [Eqs. (1) and (2)] assumes ideal and symmetric conditions whereas experiment is always subject to some error in the position and intensity of the excitation spots, and additionally sample disorder which cannot be avoided. Second, we have only included a phenomonological energy relaxation mechanism Λ for simplicity whereas better agreement between observations and theory can possibly be achieved by including directly the dynamics of the exciton reservoir into the energy relaxation of the polaritons [69].

Our experimental and numerical observations provide strong evidence of the presence of stable polariton currents resulting in discrete vortices of winding numbers $|m| \geq 1$ appearing spontaneously in odd numbered polygon structures of exciton-polariton condensates. Controlling the size of the polygon allows one to tune the coupling between condensates from being in-phase locked to anti-phase locked. In the latter, for an odd numbered polygon, the combined effects of antibonding frustration and parity symmetry breaking leads to the formation of circulating polariton currents along the polygon's edge, causing the presence of vortices at the centre with winding number $|m| \leq (N-1)/2$ where N is the number of condensates (vertices) in the polygon. The future outlook for these circulating currents can involve tuning the geometry and the profile of the excitation beams such as to effectively control the amount of the circulating polariton fluid, its tangential and inward radial velocities fields, and even the density of the condensate residing in the central region of the polygon around the core of the vortex. Thus, providing an flexible platform to study light-matter vorticity.

DATA AVAILABILITY

ACKNOWLEDGEMENTS

AUTHOR CONTRIBUTIONS

N.G.B. and P.G.L. designed the research. T.C., J.D.T., S.A., M.S. and P.G.L. performed the experiments and analysed the experimental data. W.L. and P.G.L. contributed to the design and fabrication of the microcavity. H.S. contributed on the numeric simulations and Bloch analysis. K.K. and N.G.B. contributed on the theoretical calculations. The manuscript was written through contributions from all authors. All authors have given approval to the final version of the manuscript.

ADDITIONAL INFORMATION

The authors declare no competing financial interests.

---

[1] Pismen, L. M. *Vortices in Nonlinear Fields* (Clarendon, Oxford, UK, 1999).

[2] Thouless, D. J. & Anglin, J. R. Vortex mass in a superfluid at low frequencies. *Phys. Rev. Lett.* **99,** 105301 (2007).

[3] Thouless, D. J., Ao, P. & Niu, Q. Transverse force on a quantized vortex in a superfluid. *Phys. Rev. Lett.* **76,** 3758 (1996).

[4] Klein, A., Aleiner, I. L. & Agam, O. The internal structure of a vortex in a two-dimensional superfluid with long healing length and its implications. *Annals of Physics* **346,** 195229 (2014).

[5] Leanhardt, A.E. et al. Imprinting Vortices in a Bose-Einstein Condensate using Topological Phases. *Phys. Rev. Lett.*, **89**, 190403 (2002)

[6] Engels, P., Coddington, I., Haljan, P. C., Schweikhard, V. & Cornell, E. A. Observation of long-lived vortex aggregates in rapidly rotating Bose-Einstein condensates. *Phys. Rev. Lett.* **90,** 170405 (2003).

[7] Andersen M. F., Ryu C., Clad Pierre, Natarajan Vasant, Vaziri A., Helmerson K., and Phillips W. D., Quantized Rotation of Atoms from Photons with Orbital Angular Momentum. *Phys. Rev. Lett.* **97**, 170406 (2006)

[8] Kasamatsu, K., Tsubota, M. & Ueda, M. Giant hole and circular superflow in a fast rotating Bose-Einstein condensate. *Phys. Rev. A* **66,** 053606 (2002).

[9] Aronson, I. S. & Steinberg, V. Stability of multicharged vortices in a model of superflow. *Phys. Rev. B* **53,** 75 (1996).

[10] Shin, Y. et al. Dynamical Instability of a Doubly Quantized Vortex in a Bose–Einstein Condensate. *Phys. Rev. Lett.*, **93**, 160406 (2004)

[11] Telles G.D., Tavares P.E.S., Fritsch A.R., Cidrim A., Bagnato V.S., White A.C., Allen A.J., Barenghi C.F., Twisted unwinding of multi-charged quantum vortex and generation of turbulence in atomic Bose-Einstein condensates *arXiv:1505.00616v2* (2015)

[12] Yang, S. J., Wu, Q. S., Zhang, S. N. & Feng, S. Giant vortex and skyrmion in a rotating two-species Bose-Einstein condensate. *Phys. Rev. A* **77,** 033621 (2008).

[13] Wang, D. S., Song, S. W., Xiong, B. & Liu, W. M. Quantized vortices in a rotating Bose-Einstein condensate with spatiotemporally modulated interaction. *Phys. Rev. A* **84,** 053607 (2011).

[14] Zhou, X. F., Zhou, J. & Wu, C. Vortex structures of rotating spin-orbit-coupled Bose-Einstein condensates. *Phys. Rev. A* **84,** 063624 (2011).

[15] Bretin, V., Stock, S., Seurin, Y. & Dalibard, J. Fast rotation of a Bose-Einstein condensate. *Phys. Rev. Lett.* **92,** 050403 (2004).

[16] Blaauwgeers, R. et al. Double-quantum vortex in superfluid 3He-A. *Nature* **404,** 471-473 (2000).

[17] Baelus, B. J. & Peeters, F. M. Dependence of the vortex configuration on the geometry of mesoscopic flat samples. *Phys. Rev. B* **65,** 104515 (2002).

[18] Moshchalkov, V. V., Qiu, X. G. & Bruyndoncx, V. Paramagnetic Meissner effect from the self-consistent solution of the Ginzburg-Landau equations. *Phys. Rev. B* **55,** 11793 (1997).

[19] Bruyndoncx, V. et al. Giant vortex state in perforated aluminum microsquares. *Phys. Rev. B* **60,** 4285 (1999).

[20] Kanda, A., Baelus, B. J., Peeters, F. M., Kadowaki, K. & Ootuka, Y. Experimental evidence for giant vortex states in a mesoscopic superconducting disk. *Phys. Rev. Lett.* **93,** 257002 (2004).

[21] Grigorieva, I. V. et al. Pinning-induced formation of vortex clusters and giant vortices in mesoscopic superconducting disks. *Phys. Rev. Lett.* **99,** 147003 (2007).

[22] Kramer, R. B. G., Silhanek, A. V., Van de Vondel, J., Raes, B. & Moshchalkov, V. V. Symmetry-induced giant vortex state in a superconducting Pb film with a fivefold penrose array of magnetic pinning centers. *Phys. Rev. Lett.* **103,** 067007 (2009).

[23] Cren, T., Serrier-Garcia, L., Debontridder, F. & Roditchev, D. Vortex fusion and giant vortex states in confined superconducting condensates. *Phys. Rev. Lett.* **107,** 097202 (2011).

[24] Neshev, D. et al. Observation of discrete vortex solitons in optically induced photonic lattices. *Phys. Rev. Lett.* **92,** 123903 (2004).

[25] Fleischer, J. W. et al. Observation of vortex-ring "discrete" solitons in 2D photonic lattices. *Phys. Rev. Lett.* **92,** 123904 (2004).

[26] Ostrovskaya, E. A. & Kivshar, Yu. S. Matter-wave gap vortices in optical lattices. *Phys. Rev. Lett.* **93,** 160405 (2004).

[27] Terhalle, B. et al. Observation of multivortex solitons in photonic lattices. *Phys. Rev. Lett.* **101**, 013903 (2008).

[28] Terhalle, B., *et. al.* Observation of double-charge discrete vortex solitons in hexagonal photonic lattices. *Phys. Rev. A* **79**, 043821 (2009).

[29] Pal, V. et al. Phase locking of even and odd number of lasers on a ring geometry: effects of topological-charge. *Opt. Express* **18,** 13041 (2015).

[30] Pal, V. et al. Observing Dissipative Topological Defects with Coupled Lasers. *Phys. Rev. Lett.* **119,** 013902 (2017).

[31] Tamate, S., Yamamoto, Y., Marandi, A., McMahon, P. & Utsunomiya, S. Simulating the classical XY model with a laser network. *arxiv [physics.optics]* 1608.00358 (2016).

[32] Alperin, N. S. & Berloff, N. G. Spontaneous Rotation, Multiply Charged Vortices, and the Kelvin-Helmholtz Instability in Nonconservative Trapped Bose Condensates. *arxiv nlin.PS* 2001.10314 (2020).

[33] Biondi, M., et al. Incompressible Polaritons in a Flat Band. *Phys. Rev. Lett.* **115,** 143601 (2015).

[34] Wannier G. H. Antiferromagnetism. The Triangular Ising Net. *Phys. Rev.* **97**, 357 (1950).

[35] Bramwell, S. T. & Harris, J. M. Frustration in Ising-type spin models on the pyrochlore lattice. *J. Phys.: Condens. Matter* **10**, L215 (1998).

[36] Struck, J., et al. Quantum Simulation of Frustrated Classical Magnetism in Triangular Optical Lattices. *Science* **333**, 996 (2011).

[37] Nixon, M., et al. Observing Geometric Frustration with Thousands of Coupled Lasers. *Phys. Rev. Lett.* **110**, 184102 (2013).

[38] Baboux, F. and Ge, L. and Jacqmin, T. and Biondi, M. and Galopin, E. and Lemaître, A. and Le Gratiet, L. and Sagnes, I. and Schmidt, S. and Türeci, H. E. and Amo, A. and Bloch, J. Bosonic Condensation and Disorder-Induced Localization in a Flat Band. *Phys. Rev. Lett.*, **116**, 066402 (2016).

[39] Kasprzak, J. et al. Bose-Einstein condensation of exciton polaritons. *Nature* **443,** 409 (2006).

[40] Keeling, J. & Berloff, N. G. Exciton-polariton condensation. *Contemporary Physics* **52,** 131 (2011).

[41] Carusotto, I. & Ciuti, C. Quantum fluids of light. *Rev. of Mod. Phys.* **85,** 299 (2013).

[42] Lagoudakis, K. G. et al. Quantized vortices in an exciton-polariton condensate. *Nat. Phys.* **4**, 706 (2008).

[43] Sanvitto, D. et al. Persistent currents and quantized vortices in a polariton superfluid. *Nat. Phys.* **6**, 527 (2010).

[44] Krizhanovskii, D. N. et al. Effect of interactions on vortices in a nonequilibrium polariton condensate. *Phys. Rev. Lett.* **104**, 126402 (2010).

[45] Antón, C., Tosi, G., Martín, M. D., Viña, L., Lemaître, A., and Bloch, J., Role of supercurrents on vortices formation in polariton condensates. *Optics Express* **20**, 16366 (2012).

[46] Robert Dall, Michael D. Fraser, Anton S. Desyatnikov, Guangyao Li, Sebastian Brodbeck, Martin Kamp, Christian Schneider, Sven Höfling, and Elena A. Ostrovskaya, Creation of Orbital Angular Momentum States with Chiral Polaritonic Lenses. *Phys. Rev. Lett.* **113**, 200404

(2014).

[47] H. Sigurdsson, X. Ma, O. A. Egorov, I. A. Shelykh, and T. C. H. Liew, Information processing with topologically protected vortex memories in exciton-polariton condensates. *Phys. Rev. B* **90**, 014504 (2014).

[48] Gao, T., Li, G., Estrecho, E., Liew, T. C. H., Comber-Todd, D., Nalitov, A. V., Steger, M., West, K., Pfeiffer, L., Snoke, D. W., Kavokin, A. V., Truscott, A. G., and Ostrovskaya, E. A. Chiral Modes at Exceptional Points in Exciton-Polariton Quantum Fluids. *Phys. Rev. Lett.* **120**, 065301 (2018).

[49] Yulin, A. V., Nalitov, A. V., and Shelykh, I. A. Spinning polariton vortices with magnetic field. *Phys. Rev. B* **101**, 104308 (2020).

[50] Ma, X., Berger, B., Aßmann, M., Driben, R., Meier, T., Schneider, C., Höfling, S., and Schumacher, S. Realisation of all-optical vortex switching in exciton-polariton condensates. *Nat. Comms.* **11**, 897 (2020).

[51] Barkhausen, F., Schumacher, S., and Ma, X. Multistable circular currents of polariton condensates trapped in ring potential. *Optics Letters* **45**, 1192 (2020).

[52] Ma, X. and Schumacher, S. Vortex Multistability and Bessel Vortices in Polariton Condensates. *Phys. Rev. Lett.* **121**, 227404 (2018).

[53] Töpfer, J. D., Sigurdsson, H., Pickup, L., and Lagoudakis, P. G. Time-delay polaritonics. *Commun. Phys.* **3**, 2 (2019).

[54] Ohadi, H. et al. Nontrivial phase coupling in polariton multiplets. *Phys. Rev. X* **6,** 031032 (2016).

[55] Berloff, N.G., Silva, M., Kalinin, K., Askitopoulos, A., Töpfer, J.D., Cilibrizzi, P., Langbein, W., & Lagoudakis, P.G. Realizing the classical XY Hamiltonian in polariton simulators. *Nature Materials* **16**, 1120 (2017).

[56] Kim, N. Y., Kusudo, K., Wu, C., Masumoto, N., Löffler, A., Höfling, S., Kumada, N., Worschech, L., Forchel, A. and Yamamoto, Y. Dynamical d-wave condensation of exciton-polaritons in a two-dimensional square-lattice potential. *Nature Physics* **7**, 681 (2011).

[57] Krizhanovskii, D. N., Lagoudakis, K. G., Wouters, M., Pietka, B., Bradley, R. A., Guda, K., Whittaker, D. M., Skolnick, M. S., Deveaud-Plédran, B., Richard, M., André, R. and Dang, Le Si Coexisting nonequilibrium condensates with long-range spatial coherence in semiconductor microcavities. *Phys. Rev. B* **80**, 045317 (2009).

[58] Ohadi, H., Dreismann, A., Rubo, Y. G., Pinsker, F., del Valle-Inclan Redondo, Y., Tsintzos, S. I., Hatzopoulos, Z., Savvidis, P. G. and Baumberg, J. J. Spontaneous Spin Bifurcations and Ferromagnetic Phase Transitions in a Spinor Exciton-Polariton Condensate. *Phys. Rev. X* **5**, 031002 (2015).

[59] Aleiner, I. L., Altshuler, B. L., and Rubo, Y. G. Radiative coupling and weak lasing of exciton-polariton condensates. *Phys. Rev. B* **85**, 121301 (2012).

[60] Nalitov, A. V., Liew, T. C. H., Kavokin, A. V., Altshuler, B. L. and Rubo, Y. G. Spontaneous Polariton Currents in Periodic Lateral Chains. *Phys. Rev. Lett.* **119**, 067406 (2017).

[61] Nalitov, A. V., Sigurdsson, H., Morina, S., Krivosenko, Y. S., Iorsh, I. V., Rubo, Y. G., Kavokin, A. V. and Shelykh, I. A. Optically trapped polariton condensates as semiclassical time crystals. *Phys. Rev. A*, **99**, 033830 (2019).

[62] Cilibrizzi, P., et al. Polariton condensation in a strain-compensated planar microcavity with InGaAs quantum wells *Applied Physics Letters* **105**, 191118 (2014).

[63] Wouters, M. & Carusotto, I. Excitations in a nonequilibrium Bose-Einstein condensate of exciton polaritons. *Phys. Rev. Lett.* **99,** 140402 (2007).

[64] Keeling, J. & Berloff, N. G. Spontaneous rotating vortex lattices in a pumped decaying condensate. *Phys. Rev. Lett.* **100,** 250401 (2008).

[65] Berloff, N.G. & Keeling, J. Universality in modelling non-equilibrium polariton condensates. Book chapter in "Quantum Fluids: hot-topics and new trends", eds. A. Bramati and M. Modugno (Springer-Verlag, 2013).

[66] Pal, V., Mahler, S., Tradonsky, C., Friesem, A. A. & Davidson, N. Rapid fair sampling of XY spin Hamiltonian with a laser simulator *arXiv physics.optics* 1912.10689 (2019)

[67] Mikko Möttönen, Ville Pietilä, and Sami M. M. Virtanen, Vortex Pump for Dilute Bose-Einstein Condensates. *Phys. Rev. Lett.* **99**, 250406 (2007)

[68] C. Ryu, M. F. Andersen, P. Clad, Vasant Natarajan, K. Helmerson, and W. D. Phillips, Observation of Persistent Flow of a Bose-Einstein Condensate in a Toroidal Trap. *Phys. Rev. Lett.* **99**, 260401 (2007)

[69] M. Wouters, T. C. H. Liew, and V. Savona, Energy relaxation in one-dimensional polariton condensates. *Phys. Rev. B* **82**, 245315 (2010).

Observation of giant discrete vortices in exciton-polariton polygon condensates: Supplementary Information

I.   SAMPLE & EXPERIMENTAL METHODS

The semiconductor microcavity structure studied here is a planar, strain compensated 2λ GaAs microcavity with embedded InGaAs quantum wells (QWs). Strain compensation was achieved by $AlAs_{0.98}P_{0.02}$/GaAs distributed Bragg reflector layers instead of the thin AlP inserts in the AlAs layers used in Ref. [S1] as their effective composition could be better controlled. The bottom distributed Bragg reflector consists of 26 pairs of GaAs and $AlAs_{0.98}P_{0.02}$ while the top has 23 of these pairs, resulting in very high reflectance ($>99.9\%$) in the stop-band region of the spectrum. The average density of hatches along the [110] direction was estimated from transmission imaging to be about 6/mm, while no hatches along the [1$\bar{1}$0] direction were observed. Three pairs of 6 nm $In_{0.08}Ga_{0.92}As$ QWs are embedded in the GaAs cavity at the anti-nodes of the field as well as two additional QWs at the first and last node to serve as carrier collection wells. The large number of QWs was chosen to increase the Rabi splitting and keep the exciton density per QW below the Mott density [S2] also for sufficiently high polariton densities to achieve polariton condensation under non-resonant excitation. The strong coupling between the exciton resonance and the cavity mode is observed with a vacuum Rabi-splitting of $2\hbar\Omega \sim 8$ meV. A wedge in the cavity thickness allows access to a wide range of exciton-cavity detuning. All measurements reported here are taken at $\Delta \approx -5.5$ meV. The measured Q-factor is ~ 12000, while the calculated bare cavity Q-factor, neglecting in-plane disorder and residual absorption, is ~ 25000. As the emission energy of the InGaAs QWs is lower than the absorption of the GaAs substrate, we can study the photoluminescence (PL) of the sample both in reflection and transmission geometry. The transmission geometry, which is not available for GaAs QWs, allows us to filter the surface reflection of the excitation, and has been widely utilised to probe the features of polariton fluids [S3, S4] under resonant excitation of polaritons. Using real and Fourier space imaging under non-resonant optical excitation, polariton condensation, and a second threshold marking the onset of photon lasing, i.e. the transition from the strong to the weak-coupling regime, was studied in this microcavity [S5].

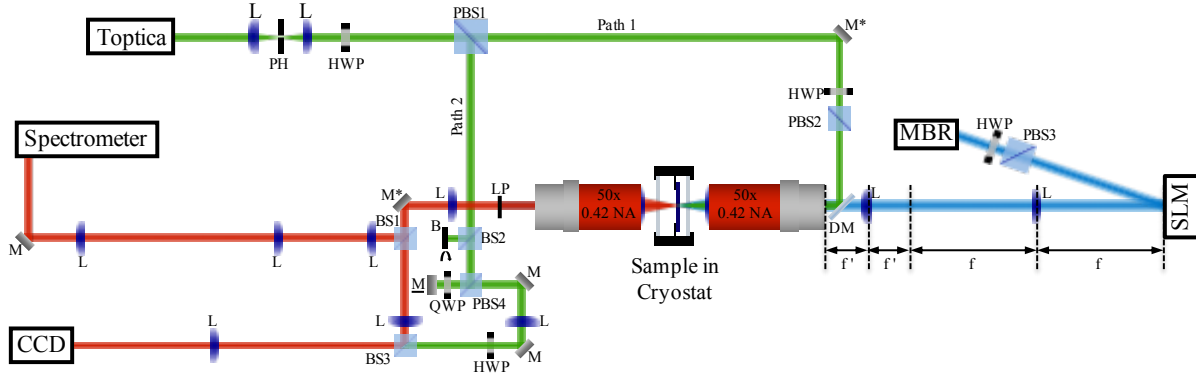In the experiments described here the sample was held in a cold finger cryostat at a

FIG. S1. Experimental set up: mirrors (M, M*(periscope), <u>M</u> (mounted on translation stage), DM (dichroic mirror)); lenses (L); polarising beamsplitter (PBS); non-polarising beamsplitter (NPBS); half-wave plate (HWP); quarter-wave plate (QWP); long-pass filter (LP); and beam block (B). Simultaneously, real-space PL is detected onto the uncoupled CCD and 2D Fourier space is projected onto the spectrometer allowing us to view either the 2D Fourier space or the energy resolved dispersion by using the grating. The external seed laser is brought to be resonant with the PL by going on the grating and detecting the PL from BS1 and the laser by removing block (B) in front of BS2 and tuning the external laser. For the homodyne interferometry, the external seed laser is split before the sample, along path 1, a small amount seeds one of the condensates, whilst along path 2, the remainder is interfered with the PL on BS3. The path of the external seed laser is shown in green, the PL is shown in red, and the excitation laser is shown in blue.

temperature of $T \approx 4\,\mathrm{K}$. Continuous wave (CW) excitation is provided by a single mode Ti:Sapphire laser modulated by an acousto-optic modulator (AOM) to form a quasi-CW beam. We use non-resonant excitation from the epi side and utilise two different detections schemes schemes: detect the emission from the substrate side so that the excitation is filtered by the absorption of the GaAs substrate (transmission geometry), or detect the emission from the epi side to prevent disruption of the Fourier space imaging (reflection geometry). The optical excitation, for all the measurements reported in this work, is at the first reflectivity minimum above the cavity stop band. The spatial profile of the excitation beam is modulated to a regular polygon with Gaussian profiles at each vertex of approximately equal in diameter spots using a reflective spatial light modulator (SLM). We use high numerical aperture microscope objectives ($0.4 \leq \mathrm{NA} \leq 0.5$) to focus the spatially modulated beam to $\sim$1-2$\,\mu$m in diameter, at full width at half maximum, excitation spots and to collect the PL in

reflection geometry. The PL from the sample can also be collected in transmission geometry with $\pm 25°$ collection angle, by a 0.42 NA microscope objective. The resonant seed laser (Toptica) mode is first cleaned with pinhole (PH) to ensure a clean phase front. Then the seed laser is split into two paths at PBS1 with a small amount down path 1, directed onto the sample using a dichroic mirror (DM) which passes the excitation laser but reflects the PL wavelength; and the rest down path 2 where the laser is interfered with the PL on BS3 for homodyne interferometry. The remainder of the excitation laser is filtered with a long pass filter (LP) and the paths are brought to zero time delay by controlling mirror $\underline{\text{M}}$ which is on a linear translational stage. Two-dimensional Fourier and real-space PL imaging are obtained by projecting the corresponding space onto a cooled charge-coupled device (CCD) camera.

Initially, we viewed the system by time averaging over multiple instances of the condensate to obtain real- and Fourier-space images. The PL is then directed at a second SLM (not shown) where the hologram design allowed us to investigate the first-order mutual coherence function between any two condensates from the polygon [S6]. The selected PL was projected onto a CCD in Fourier-space so that the mutual coherence between the two condensates under investigation could be seen in the resultant interferogram. The magnitude of the $|g^{(1)}|$ is extracted from the interferograms by fitting with

$$I_{\text{int}} = I_1 + I_2 + 2\sqrt{I_1 I_2}|g^{(1)}| \cos{(kx + \theta)}, \tag{S1}$$

where I_{int}, I_1 and I_2 are read from line profiles along a direction x taken across the images of the interference, reference arm 1, and reference arm 2, respectively [S7]. The fitting parameters are the phase (θ), wavenumber (k) and coherence magnitude ($|g^{(1)}|$), allowing us to directly extract the phase and coherence for each dataset.

Since the phases across the polygon cannot be measured directly, we utilise homodyne interferometry [S8] (see Fig. S1). We seed one of the condensates with part of an external laser (Toptica) which is tuned to be resonant with the condensate. The external seed perturbs the condensate to the frequency of the seed laser, by utilising the U(1) symmetry breaking at the point of condensation, without interfering with the dissipative dynamics of the condensate. The PL is then interfered with the remainder of the external seed laser on the third non-polarising beam splitter (BS3). We then use off-axis digital holography [S9] to extract both magnitude and phase of the condensate order parameter Ψ at the resonance

energy $\hbar\omega$ of the seed laser. Furthermore, to view a single instance of the condensate, we trigger the AOM once, thereby creating a single instance of the condensate which is $20 - 60$ μs in length. We synchronise the CCDs detecting real-, Fourier-space and energy resolved dispersion to the AOM thereby ensuring that the CCDs record the entirety of each instance of the condensate.

II.   2D GROSS-PITAEVSKII SIMULATION PARAMETERS

The values for the parameters appearing in Equations (1) and (2) to simulate the two-dimensional driven-dissipative Gross-Pitaevskii equation are specified here. The polariton mass and lifetime are based on the sample properties: $m^* = 0.35$ meV ps^2 μm^{-2} and $\gamma^{-1} = 5.5$ ps. We choose values of interaction strengths typical of GaAs based systems: $\alpha = 3.3$ μeV μm^2 and $g = 2\alpha$. The redistribution rate of reservoir excitons is taken here as comparable to the condensate decay rate $\Gamma^{-1} = 5$ ps and the damping parameter is chosen small $\Lambda = 0.05$. The final two parameters are found by fitting numerical results to experiment which gives $\hbar R = 33$ μeV μm^{-2}, and $G = 66$ μeV μm^{-2}. The n-th pump element (vertex) is written as a Gaussian profile $P_n(\mathbf{r}) = P_0 e^{-r_n^2/2w_{\mathrm{RMS}}^2}$ where $r_n = \sqrt{(x - x_n)^2 + (y - y_n)^2}$, and (x_n, y_n) denote the coordinates of the element. Here P_0 denotes the pump power density, and $w_{\mathrm{RMS}} = 1.27$ μm the RMS width (corresponds to a 3 μm full-width-half-maximum), slightly larger than the incident light beam width in order to account for the small diffusion of excitons from the pump spots.

III.   EXPERIMENTAL NON-VORTEX CONFIGURATIONS

Condensate octagon and decagon geometries are displayed in Fig. S2, synchronised in in-phase (left hand side) and anti-phase (right hand side) configuration with respect to nearest-neighbour condensates. The in-phase states in Figs. S2(a,g) show the real-space configuration with an odd number of fringes between nearest neighbour condensates (in this case three fringes). In real- (Figs. S2(a,g)) and Fourier-space (Figs. S2(b,h)) both display a bright spot at the centre indicating that all spots are in-phase. The phase in Figs. S2(c,i) reflect the clear pattern in the real-space and it can be seen that the spot centres are all at the same phase. Conversely, the anti-phase configurations have a dark spot at the centre
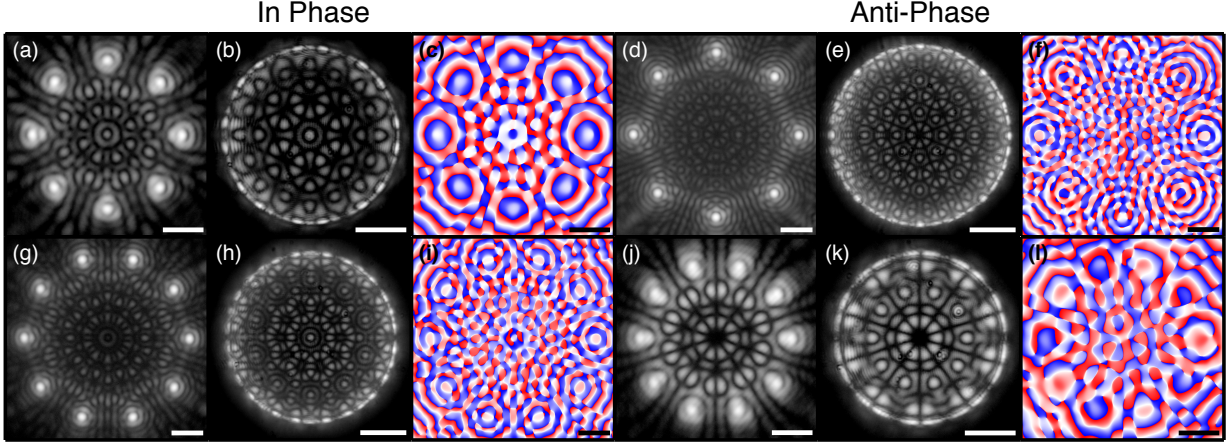
FIG. S2. Real- (a,d), Fourier-space PL (b,e), and real-space phase (c,f) of an octagon condensate in in-phase and anti-phase configurations. (g-l) Same measurements for a decagon condensate. The real and Fourier space PL is time-averaged and displayed on a log scale between 0.01 and 1. The phase is extracted from time-averaged interferograms with off-axis digital holography.

and display clear radial nodal lines in real- Figs. S2(d,j) and Fourier-space Figs. S2(e,k). The corresponding polariton phase maps are shown in Figs. S2 (f,l), where neighbouring spots can be clearly observed in anti-phase.

Similarly, in the non-frustrated regime ($J > 0$) odd numbered pump polygons will form condensates in the in-phase configuration. The in-phase state has a bright fringe between adjacent condensates as well as the bright central fringe in both real- and Fourier-space images, as shown in Figs. S3(a,b,d,e,g,h) for a pentagon, heptagon and nonagon, respectively. The corresponding polariton phase maps are shown in Figs. S3(c,f,i), where the neighbouring spots can be seen to be in-phase.

IV. SIMULATED VORTEX FORMATION STATISTICS

In Fig. S4(a) (red dot-dashed curve) we show the probability of a $|m| = 2$ vortex forming in a pentagon geometry by simulating Eq. (1) from stochastic initial conditions, averaged over 30 realisations (Monte-Carlo methods). The horizontal axis represents the short distance d between neighbours (edge length) which is related to the polygons radius R through the formula $d = 2R \sin(\pi/N)$. Between the regions of vortex formation, the probability of in-phase solutions (blue curve) forming becomes dominant as expected. The probability is
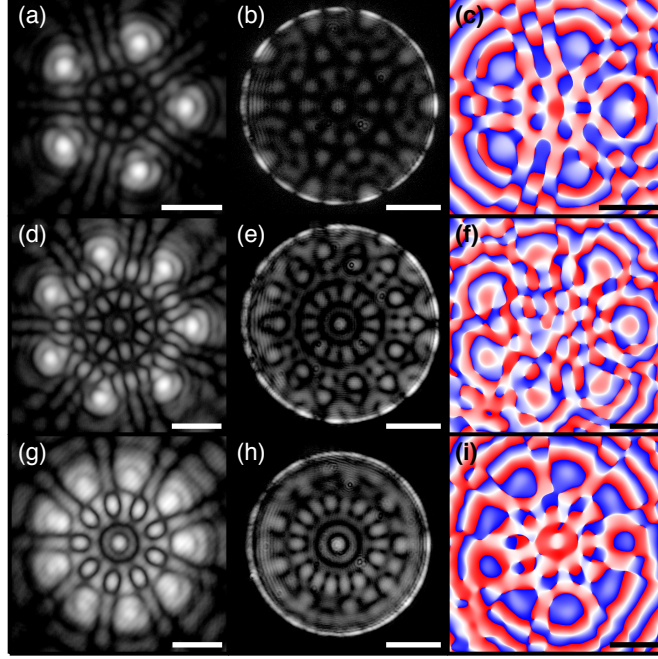
FIG. S3. Real- (a), Fourier-space PL (b), and real-space phase (c) of a pentagon in in-phase configuration. Same measurements are shown for heptagon (d-f) and nonagon condensates (g-i). Real- and Fourier-space PL is time-averaged and displayed on a log scale between 0.01 and 1. The phase is extracted from time-averaged interferograms with off-axis digital holography.

estimated from the root-mean-square error of the condensate phase at each vertex,

$$\text{ERR}(\bar{\theta}) = \sqrt{\frac{1}{2N} \left[\sum_{n=1}^{N} (\cos(\bar{\theta}) - \cos(\theta_{n,n+1}))^2 + (\sin(\bar{\theta}) - \sin(\theta_{n,n+1}))^2 \right]}. \quad \text{(S2)}$$

Here $\bar{\theta}$ is the expected phase configuration (e.g., $\bar{\theta} = 0$ for in-phase configuration). At the end of each simulation we classify the formation of the expected state successful when $\text{ERR}(\bar{\theta}) \leq 0.05$. The probability is then calculated as the number of successful formations over number of realisations. In Fig. S4(b) we show the probability of in-phase (blue whole line) and anti-phase (red dot-dashed line) configurations forming in a polygon of $N = 6$. The results evidence that non-frustrated polygons have step-like domain walls separating the regimes of in-phase and anti-phase configurations. This is in contrast to the frustrated (e.g., $N = 5$) polygons shown in Fig. S4(a) where the vortex formation probability follows a more complex distribution.

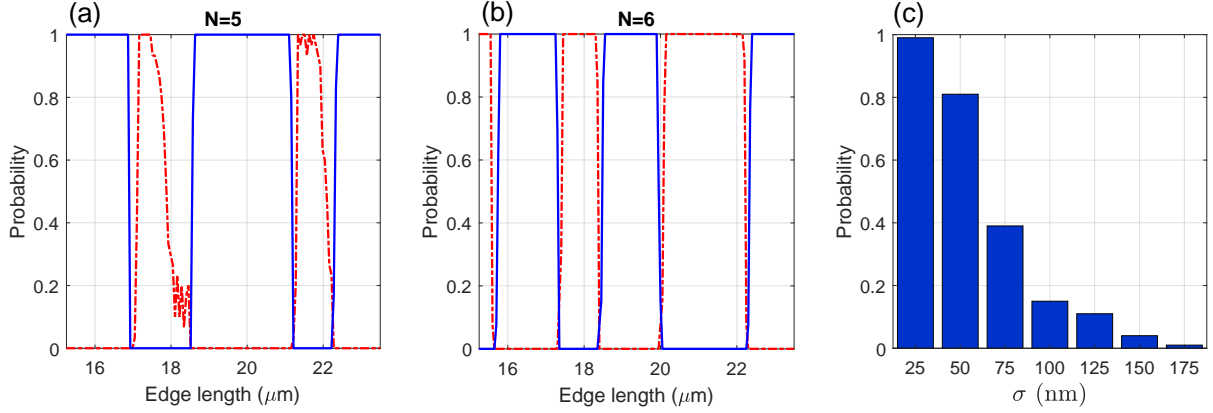We also investigate the formation probability of a $|m| = 2$ vortex state for non-ideal

6

FIG. S4. (a) Simulated probability of $|m| = 2$ vortex formation (red dot-dashed line) against probability of in-phase configuration (blue whole line) using Eq. (1) for a pentagon pumping geometry. The average is done over 30 realisations of stochastic initial conditions. The horizontal axis denotes the short distance between condensates (the edges of the polygon). (b) Simulated probability of an anti-phase formation (red dot-dashed line) against probability of in-phase configuration (blue whole line) using Eq. (1) for a hexagon pumping geometry. (c) Probability of $|m| = 2$ vortex formation for increasing standard deviation in the randomly displaced vertex coordinates of the pentagon.

pentagons. We introduce uncertainties to the coordinates of each pump vertex written $(x_n + dx, \ y_n + dy)$. Here, dx, dy are normally distributed random variables with zero mean and standard deviation σ. In Fig. S4(c) we show the drop in probability of the $|m| = 2$ vortex forming for increasing standard deviation. These results carry an important message. As the the number of pump spots increases the probability of maintaining a perfectly regular polygon drops since experimental uncertainties are never fully avoided, and therefore the probability of observing a vortex state diminishes. This challenge should then be overcome by either designing an alternative discrete rotational geometry which favours more strongly the formation of vortex states, or through future design of higher quality experiments.

V.   RADIUS SCAN OF HEPTAGON

A scan of the radius of a heptagon was performed whilst integrating over multiple instances of the condensate as the real-space shows in Fig. S5. The system was found to

7

be quite robust and stable over the course of the measurement. The system is initially in the "fifth" in-phase configuration at 19.81 μm corresponding to five bright fringes observed between neighbouring condensates and a bright notch at the centre. Upon increasing the radius, the system alters whilst it does retain five fringes between vertices, the centre now has a small dark notch surrounded by a bright ring, most clearly seen at a radius of 21.12 μm corresponding to the first vortex state forming. Further increase of the radius caused the state to fracture one or more of the condensates similar to the vortex-antivortex state demonstrated in Fig. 5. Furthermore, at a radius of 22.53 μm, two of the condensates can be seen in the integrated real-space to be splitting (middle left-hand and bottom left-hand condensates), indicative that the frustration in the polygon has caused some of the condensates to split. A different number of fringes can be seen between different vertices (either five or six).

The next state to occur is seen at 23.29 μm with six fringes between vertices, where the real-space pattern has a heptagon at its centre surrounding a dark notch, (Fig. S5, fourth row, second image). The heptagon pattern in real-space comes from several instances of both $+\theta_{i,i+1}$ and $-\theta_{i,i+1}$ being time integrated causing a merging of the patterns and reduced visibility in the fringes. The heptagon then eventually returns to in-phase configuration at a radius of 24.38 μm with seven fringes between neighbouring condensates (Fig. S5, bottom row, third image).

VI. IMAGE PARAMETERS

We have used two colour scales to display the data in this work. The scaling in each figure is such that it display's the data clearly and is listed below per figure.

Figure 1: The real- and Fourier-space is displayed in false, logarithmic greyscale and saturated between 0.001-1 (d,e,j,k) and 0.01-1 (g,h,m,n). The phase is displayed in a linear Red-White-Blue scale between 0 and 2π (f,j,l,o). The scale bars represent 10 μm (d,f,g,i,j,l,m,o), and 1 μm^{-1} (e,h,k,n).

Figure 2: The real- and Fourier-space is displayed in false, logarithmic greyscale and saturated between 0.005-1. The scale bars represent 10 μm row (a), and 1 μm^{-1} row (b).

Figure 3: The real- and Fourier-space is displayed in false, logarithmic greyscale and saturated between 0.01-1 (a,b,e,f). The phase is displayed in a linear Red-White-Blue scale
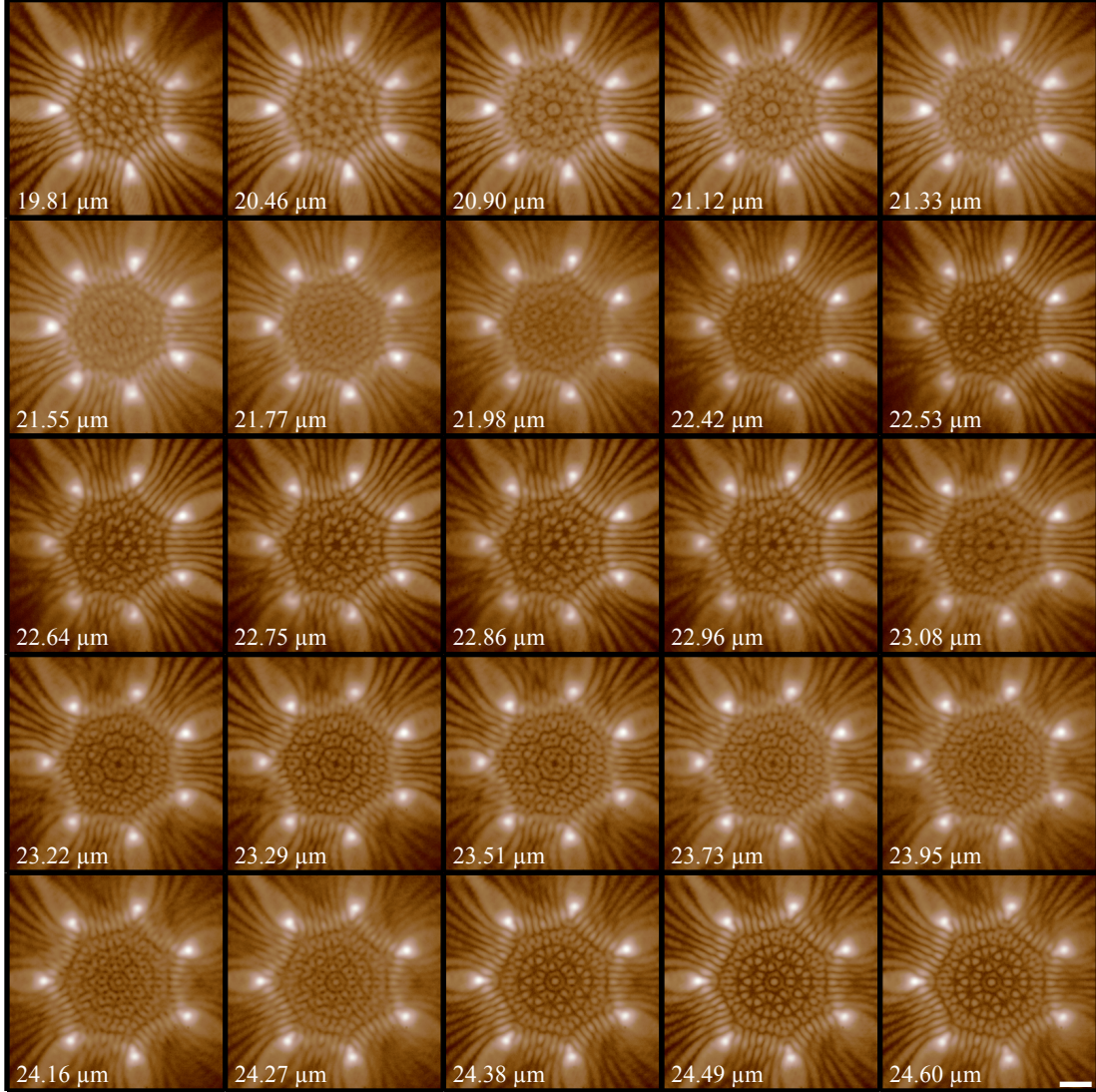
8

FIG. S5. Increasing the radius of a heptagon from ∼ 19.81 μm to ∼ 24.6 μm. The normalised real-space can be seen to go from in-phase with five fringes between neighbouring condensates at 19.81 μm; to the first vortex state at 21.12 μm; to the second vortex state at 23.29 μm; and back to in-phase at 24.38 μm, where seven fringes can be seen between neighbouring condensates. Between these states there are several fractured states. The third vortex state, which would contain a three-fold vortex with a full phase rotation of 6π was not observed in this run.

between 0 and 2π (c,d,g,h). The scale bars represent 10 μm (a,c,e,g), 1 μm (d,h), and 1 μm^{-1}, (b,f).

Figure 4: The real- and Fourier-space is displayed in false, logarithmic greyscale and saturated between 0.01-1 (a,e,f), and 0.07-0.12 (b). The phase is displayed in a linear Red-

9

White-Blue scale between 0 and 2π (c,d,g,h). The scale bars represent 10 μm (a,c,e,g), 5 μm (b), 1 μm (d,h), and 1 μm^{-1} (f).

Figure 5: The real- and Fourier-space is displayed in false, logarithmic greyscale and saturated between 0.05-1 (a), 0.116-0.17 (b), 0.01-1 (e,f). The phase is displayed in a linear Red-White-Blue scale between 0 and 2π (c,d,g,h). The scale bars represent 10 μm (a,c,e,g), 5 μm (b), 1 μm (d,h), and 1 μm^{-1} (f).

Figure S2: The real- and Fourier-space is displayed in false, logarithmic greyscale and saturated between 0.01-1 (a,b,e,h,j,k), 0.004-1 (g) and 0.001-1 (d). The phase is displayed in a linear Red-White-Blue scale between 0 and 2π (c,f,i,l). The scale bars represent 10 μm (a,c,d,f,g,i,j,l), and 1 μm^{-1} (c,e,h,k).

Figure S3: The real- and Fourier-space is displayed in false, logarithmic greyscale and saturated between 0.01-1 (a,b,e,g,h) and 0.04-1 (d). The phase is displayed in a linear Red-White-Blue scale between 0 and 2π (c,f,i). The scale bars represent 10 μm (a,c,d,f,g,i), and 1 μm^{-1} (c,e,h).

Figure S5: All images are displayed in logarithmic mocha colour scale saturated between 0.001 and 1 to make the low intensity fringes more visible. All images are displayed on the same scale and the scale bar in the bottom right represents 10 μm.

[S1] Zajac, J. M., Clarke, E. & Langbein, W. Suppression of cross-hatched polariton disorder in GaAs/AlAs microcavities by strain compensation. *Appl. Phys. Lett.* **101**, 041114 (2012).

[S2] Houdré, R. et al. Saturation of the strong-coupling regime in a semiconductor microcavity: Free-carrier bleaching of cavity polaritons. *Phys. Rev. B* **52**, 7810 (1995).

[S3] Sanvitto, D. et al. All-optical control of the quantum flow of a polariton condensate. *Nature Photonics* **5**, 610 (2011).

[S4] Nardin, G. et al. Hydrodynamic nucleation of quantized vortex pairs in a polariton quantum fluid. *Nature Phys.* **7**, 635 (2011).

[S5] Cilibrizzi, P. et al. Polariton condensation in a strain-compensated planar microcavity with InGaAs quantum wells. *Appl. Phys. Letts.* **105**, 191118 (2014).

[S6] Töpfer, J. D., Chatzopoulos, I., Sigurdsson, H., Cookson, T., Rubo, Y. G., and Lagoudakis, P. G., Engineering spatial coherence in lattices of polariton condensates. *Optica*, 10.1364/OP-

TICA.409976, (2021).

[S7] Scully, M. O., Suhail Zubairy, M. *Quantum Optics* (Cambridge University Press, Sep. 1997).

[S8] Alyatkin, S., Töpfer, J. D., Askitopoulos, A., Sigurdsson, H. and Lagoudakis P. G., Optical Control of Couplings in Polariton Condensate Lattices. *Phys. Rev. Lett.* **124**, 207402 (2020).

[S9] Lagoudakis, K.G. et al. Quantized vortices in an exciton-polariton condensate. *Nat. Phys.* **4**, 706 (2008).